A Fully-Focused SAR Omega-K Closed-Form Algorithm for the Sentinel-6 Radar Altimeter Methodology and Applications

Hernandez-Burgos, Sergi; Gibert, Ferran; Broquetas, Antoni; Kleinherenbrink, Marcel; De la Cruz, Adrian Flores; Gomez-Olive, Adria; Garcia-Mondejar, Albert; Aparici, Monica Roca i.

DOI
10.1109/TGRS.2024.3367544

Publication date
2024

Document Version
Final published version

Published in
IEEE Transactions on Geoscience and Remote Sensing

A Fully Focused SAR Omega-K Closed-Form Algorithm for the Sentinel-6 Radar Altimeter: Methodology and Applications

Sergi Hernández-Burgos, Ferran Gibert, Antoni Broquetas, *Member, IEEE*, Marcel Kleinherenbrink, Adrián Flores De la Cruz, Adrià Gómez-Olivé, Albert García-Mondéjar, and Mònica Roca i Aparici

***Abstract*— The 2-D frequency-based omega-K method is known to be a suitable algorithm for fully focused SAR (FF-SAR) radar altimeter processors, as its computational efficiency is much higher than equivalent time-based alternatives without much performance degradation. In this article, we provide a closed-form description of a 2-D frequency-domain omega-K algorithm specific for instruments such as Poseidon-4 onboard Sentinel-6. The processor is validated with real data from point targets and over the open ocean. Applications such as ocean swell retrieval and lead detection are demonstrated, showing the potentiality of the processor for future operational global-scale products.**

***Index Terms*— Altimetry, delay/Doppler altimetry, fully focused SAR (FF-SAR), omega-K, SAR altimetry, synthetic aperture radar (SAR).**

I. Introduction

SPACE-BASED radar altimetry has become nowadays a consolidated Earth Observation technique with a wide range of applications, such as estimating water surface elevations in coastal and inland waters [1], monitoring and forecasting river discharges and extreme flood events [2], studying the changes in snow, ice height, and sea-ice elevation in Antarctica [3], [4], estimating the contribution of ice melting to the sea level rise [5], or mapping ice elevation and elevation change using swath interferometry altimetry [6], among others.

One of the limitations of conventional radar altimeters is the along-track resolution, which is the ability to distinguish between two targets along the surface. Initial pulse-limited radar altimeters had an along-track resolution of the size of the pulse-limited footprint, which is several kilometers [7]. In modern missions such as CryoSat-2 [8], Sentinel-3 [9], or Sentinel-6 [10], this kilometer scale limitation has been overcome by transmitting pulses at high repetition frequency ensuring coherence among them, allowing for a significant increase in the number of independent looks obtained from a single scatterer on Earth, thus enabling for Doppler-based beam-forming analysis and achieving resolutions below the kilometer scale [11]. This technological advancement allows for more accurate measurements of the Earth's surface features.

The first generation of altimeters using high pulse repetition frequency (PRF) operate in closed bursts, meaning that they send groups of pulses and then await their complete reception before sending the next burst. Indeed, missions such as CryoSat-2 or Sentinel-3 operate in this way with a PRF of 19 kHz. Applying a delay/Doppler processor (DDP) [11], closed-burst processing of 64 pulses leads to azimuth resolutions of approximately 300 m for missions such as CryoSat-2 and Sentinel-3. Newer missions, such as Sentinel-6, employ a nearly continuous pulse transmission approach with a PRF of 9–10 kHz [12], which allows it to operate in an interleaved mode and eliminates the necessity of grouping pulses into bursts [13], though its high-resolution operational processor is still based on delay/Doppler. The interleaved mode maximizes the measurement precision while ensuring a connection between data from prior altimeter missions [14], [15]. It also increases the effective PRF with respect to the closed-burst mode, reducing considerably the number of replicas that appear along-track [16].

In 2017, Egido and Smith [17] introduced the fully focused synthetic aperture radar (FF-SAR) backprojection algorithm (FF-BP), which can achieve along-track resolutions of up to the theoretical maximum, approximately half the length of the antenna in the flight direction (i.e., approximately 0.5 m for Sentinel-6). While this algorithm results in an improvement of the spatial resolution of the altimeter radargram, it also comes with high execution times. Still, such an algorithm allowed to improve altimeter performance over some applications such as inland waters [18], [19] and coastal areas [20], [21], [22], also opening the door to new calibration techniques applications [23]. Faster backprojection algorithms have been introduced for traditional SAR systems [24], [25], yet their applicability to radar altimetry remains unexplored and requires further investigation.

In 2018, Guccione et al. [26] presented the 2-D frequency-domain FF-SAR algorithm, introducing a numerical solution based on the omega-K algorithm typically used in SAR

Manuscript received 21 September 2023; revised 5 January 2024 and 9 February 2024; accepted 15 February 2024. Date of publication 19 February 2024; date of current version 29 February 2024. This work was supported by the Industrial Doctorates Plan from the Secretary of Universities and Research of the Department of Business and Knowledge of the Government of Catalonia through Project SA.45217 with Expedient Number 094 under Grant Doctorats Industrials 2020. *(Corresponding author: Sergi Hernández-Burgos.)*

Sergi Hernández-Burgos is with isardSAT, S.L., 08042 Barcelona, Catalonia, and also with the Teoria del Senyal i Comunicacions, Universitat Politècnica de Catalunya, 08034 Barcelona, Catalonia (e-mail: sergi.hernandez@isardsat.cat).

Ferran Gibert, Adrián Flores De la Cruz, Adrià Gómez-Olivé, Albert García-Mondéjar, and Mònica Roca i Aparici are with isardSAT, S.L., 08042 Barcelona, Catalonia.

Antoni Broquetas is with the Teoria del Senyal i Comunicacions, Universitat Politècnica de Catalunya, 08034 Barcelona, Catalonia.

Marcel Kleinherenbrink is with the Geoscience and Remote Sensing, Technische Universiteit Delft, 2628 CD Delft, The Netherlands.

Digital Object Identifier 10.1109/TGRS.2024.3367544

imaging for the specific case of the CryoSat-2 radar altimeter, improving the computational efficiency of the FF-BP while maintaining the same level of along-track resolution. Also, in 2018, Scagliola et al. [27] presented an FF-SAR frequency-domain approach based on the range-Doppler algorithm used in SAR imaging.

In this article, we continue exploring the 2-D frequency algorithm based on the omega-K from SAR imaging for the Sentinel-6 mission, introducing a closed-form filter by assuming a hyperbolic range with respect to one scatterer, as well as making certain orbit linear assumptions, which are further explained in the methodology section. Indeed, this article aims to provide a comprehensive explanation of the mathematical development required to derive the final expression of focused single-look (SL) waveforms for ideal point targets. The central focus is to demonstrate that when ideal conditions are met, the final expression of focused SL waveforms is equivalent to the form derived through a backprojection processor, without significant precision loss while reducing drastically the execution time. Furthermore, the results obtained show the robustness of the proposed algorithm with real data, including point targets and open ocean scenarios.

The enhanced computational efficiency of the algorithm presented, along with its ability to maintain high resolution, makes it an interesting solution for applications that require improved along-track resolution with respect to DDP techniques but also processing global-scale amounts of data. Indeed, this advancement empowers the algorithm to produce local and global FF-SAR products for both scientific research and operational utilization. Since time-domain processors such as backprojection require prolonged execution durations for computing global-scale products, the FF-SAR omega-K algorithm (FF-WK) emerges as a valuable alternative. In particular, applications such as swell monitoring [28] and lead detection [29] may benefit from these algorithms.

We commence with a methodology section elaborating on the mathematical derivation of the FF-WK. The subsequent section shows the practical implementation details of the algorithm. After that, we evaluate the algorithm's performance through extensive validation in a dedicated section over point and distributed targets. Moving forward, the Results section follows, presenting the possible applications of the algorithm within real-world scenarios, such as swell retrieval for open ocean and lead detection for sea ice. The Results section also shows a comparison in terms of computational efficiency between the omega-K and the FF-BP. Following that, we discuss potential future research directions that can build upon the algorithm proposed. Finally, this article concludes with a section summarizing our findings and offering conclusions.

II. Radar Altimetry Theory

The omega-K algorithm is a well-known technique employed in SAR imaging to reduce the number of operations with respect to backprojection by making certain assumptions about orbit geometry (such as the hyperbolic range equation or constant nominal velocity) and the transmitted signal characteristics of the satellite [30]. Its key step involves employing the Fourier transform to manipulate the frequency domain in both the range and along-track dimensions, using the coherence of the radar pulses to filter a large block of echoes at once. Instead, backprojection applies to filter for each scatterer defined in a grid, incrementing substantially the number of operations needed to filter an entire surface. In this section, we present the mathematical formulation and implementation details of the omega-K algorithm tailored for the altimeter case, which shares similarities with SAR imaging missions but incorporates some design differences, such as wider synthetic apertures, nadir-pointing antenna, higher carrier frequencies, and higher pulse bandwidth. By delving into the information provided in this section, readers should gain a comprehensive understanding of the omega-K algorithm and its applications in radar altimetry. Sections IV–VI will discuss the algorithm's effectiveness and performance, accompanied by the presentation of results.

A. Transmitted and Received Signals

For technical and processing reasons, most high-range resolution radars, including altimeters, transmit chirp pulses [31], as described by the following equation:

$$s_t(t) = w_t(t)\cos\left[2\pi\left(f_c t - \frac{\alpha}{2}t^2\right)\right] \quad -\frac{T_p}{2} < t < \frac{T_p}{2} \tag{1}$$

where $w_t(t)$ represents the pulse envelope, which is usually a rectangular window (uniform energy). Moreover, f_c is the carrier frequency of the modulated signal, t is the duration within the pulse, which is in the order of microseconds, also known as fast time, and α is the chirp rate, which is defined as the ratio of the pulse bandwidth to the pulse duration: $\alpha = B/T_p$. The quadratic term in the phase signal is a representation of the linear frequency modulation of the pulse. After the transmission through a nadir-pointing antenna, the pulse travels to the Earth's surface, where part of the energy is reflected and returned back to the sensor. We can express the received signal as

$$s_r(\eta, t) = w_\eta(\eta)\; w_r(t-\tau) \cdot \cos\left[2\pi\left(f_c(t-\tau) - \frac{\alpha}{2}(t-\tau)^2\right)\right]. \tag{2}$$

In this equation, the received signal has a time delay proportional to twice the range R between the scatterer and the altimeter sensor $\tau = 2R(\eta, t)/c$, where c is the speed of light. The slow time η refers to the time relative to the position of the satellite, and it is in the order of milliseconds. The distance between the scatterer and the altimeter sensor is influenced by the position of the satellite and the relative sensor-target movement $R(\eta, t) \approx R(\eta) + v_r \cdot t$. This consideration arises from our departure from the commonly used "stop-and-go" approximation. The "stop-and-go" approach assumes that the motion of the satellite is sufficiently low during the pulse duration so that it can be considered as if the satellite is stationary. In altimetry systems, this assumption cannot be sustained due to the influence of the Doppler effect in the signal phase caused by the high-frequency carrier used for the altimeter [17]. This effect has also been explored in high-precision SAR for estimating Doppler parameters related

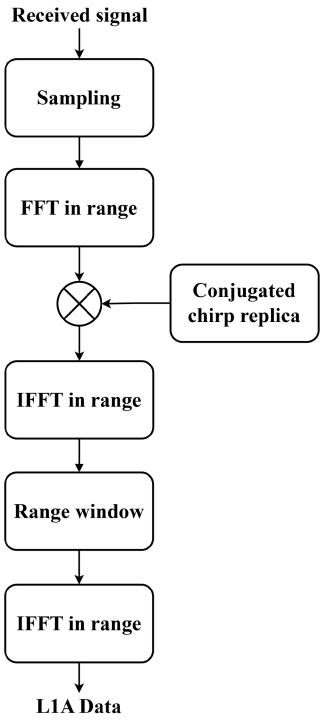

Fig. 1. Onboard Sentinel-6 radar altimeter receiver system.

to object motion [32], [33]. Furthermore, the pulse envelope $w_r(t-\tau)$ represents the received signal energy, which is affected by physical alterations that depend on the atmosphere and the Earth's surface. The along-track envelope w_η is characterized by the antenna pattern.

B. Sentinel-6 Receiver System

Fig. 1 shows the processing steps of the Sentinel-6 receiver system [34]. The signal is digitized at a very high frequency (395 MHz), after which a matched filter is applied in the frequency domain using a discrete Fourier transform (DFT) by means of the fast Fourier transform (FFT) algorithm. The matched filter is a conjugated replica of the transmitted pulse (chirp signal). The signal is then cut with a range window in the range-time domain; after that, an inverse FFT (IFFT) is applied.

The output signal for a single scatterer can be represented by the complex signal

$$S_r(\eta, f_r) = w_\eta(\eta)\, W_r(f_r) \cdot \exp\left[j2\pi \left(f_c \frac{2}{c} R(\eta) - \left(\frac{2}{c}(R(\eta) - R_{\text{trk}}) - \frac{f_d}{\alpha} \right) f_r \right) \right] \quad (3)$$

where f_r is the frequency variable in the range domain, known as the range frequency. Furthermore, the expression $f_d = 2\, f_c v_r / c$ indicates the alteration in the range of the phase due to the Doppler effect related to the relative velocity of the satellite. The term R_{trk} represents the tracker range, which is commanded onboard by the satellite. In the case of the Sentinel-6 altimeter, this range commonly refers to the central point within the range window. The satellite is moving, while chirp pulses are periodically transmitted at a designated PRF. The motion of the satellite during the slow time η results in different distances between the sensor and the scatterer for each transmitted pulse. Therefore, to accurately define the response of a target for each pulse, the range equation of the satellite with respect to the point target $R(\eta)$ must be defined.

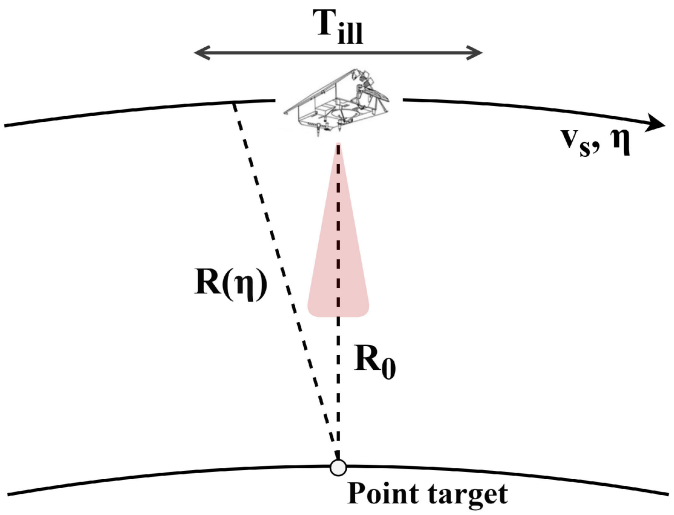

Fig. 2. Radar geometry. The satellite passes over the point target, transmitting chirp pulses periodically and receiving the echoes.

C. Radar Geometry

Fig. 2 illustrates a simplified geometry of a radar altimeter with a single scatterer in the scene. In order to determine the closed-form filter of the omega-K algorithm for the radar altimeter, some simplifications in the radar geometry are made: Earth is locally spherical of radius R_e, the satellite is moving along the track with a constant velocity v_s, and the height of the satellite and the retracker range are constant during the entire pass. The satellite is periodically transmitting pulses during a limited illumination time, T_{ill}. When a transmitted pulse reaches the Earth's surface, part of its energy is scattered back to the sensor with a delay corresponding to the satellite-scatterer distance. The equation that defines the distance of the satellite with respect to the scatterer for each instant of time is known as the range equation. In the context of Sentinel-6, we can safely express the range equation along the x-axis as a hyperbolic form [30]

$$R(x) \approx \sqrt{R_0^2 + x^2} \quad (4)$$

where R_0 is the minimum distance between the sensor and the target. The altimeter sensor has the closest range to the scatterer when $R(x=0) = R_0$. The position of the satellite x can be expressed as a function of the slow time η as follows:

$$x = \eta \cdot v_{\text{eq}} \quad (5)$$

where

$$v_{\text{eq}} \approx v_s \cdot \sqrt{\alpha_E} = v_s \cdot \sqrt{\frac{R_e}{(R_e + h)}}. \quad (6)$$

The equivalent speed v_{eq} is determined by multiplying the satellite's velocity v_s by a correction term to account for

the curvature of the Earth, the square root of the orbital factor α_E [30]. The correction term depends on the Earth's radius, denoted as R_e, and the nominal altitude of the satellite, represented as h. This velocity can also be understood as the geometric mean between the velocity of the satellite and the velocity projected on ground v_g as $v_{\text{eq}} = (v_s \cdot v_g)^{1/2}$. With these changes of variables, the range equation becomes

$$R(\eta) = \sqrt{R_0^2 + \left(\eta \cdot v_{\text{eq}}\right)^2}. \tag{7}$$

For the typical values of Sentinel-6 (Ku-band carrier frequency) and 5 s of the illumination time, the difference between the approximated range and the range computed with the telemetry data is around 4 mm in the borders of the illumination time. This range equation will be further used to derive the closed form of the 2-D frequency signal.

D. Along-Track Fourier Transform

In order to obtain the 2-D frequency signal, we need to apply the Fourier Transform in the slow time (along-track) domain to the received signal [see (3)]

$$S\left(f_\eta, f_r\right) = \int_{-\infty}^{\infty} S_r(\eta, f_r) \exp\left[-j2\pi\eta f_\eta\right] d\eta. \tag{8}$$

$S(f_\eta, f_r)$ is the 2-D frequency signal where f_η is the along-track frequency variable. This frequency variable is also called Doppler frequency. Regarding the phase of the integral, it contains quadratic terms in the slow time variable, making it challenging to obtain an analytical expression. Nevertheless, we can overcome this obstacle by applying the principle of stationary phase (POSP). The POSP enables us to analytically express integrals with quadratic modulation in their signal by locating the stationary phase point η_0 where the derivative of the phase of the integral is zero [35]. Consequently, the whole phase that requires derivation is

$$\theta(\eta) = f_c \frac{2}{c} R(\eta) - \left(\frac{2}{c}(R(\eta) - R_{\text{trk}}) - \frac{f_d(\eta)}{\alpha}\right) f_r - \eta f_\eta. \tag{9}$$

The stationary phase point η_0 can be obtained by finding the zero in the derivative of the phase defined in the latter equation

$$\left.\frac{\partial\theta(\eta)}{\partial\eta}\right|_{\eta=\eta_0} = 0. \tag{10}$$

Once we obtain the stationary phase point η_0, the 2-D frequency signal can be expressed as

$$S\left(f_\eta, f_r\right) \approx \; w_\eta(\eta_0) \cdot W_r(f_r) \cdot \exp\left[j2\pi \cdot \theta(\eta_0)\right]. \tag{11}$$

The along-track frequency-domain envelope is obtained by substituting the stationary phase point η_0 to the along-track time-domain envelope. The 2-D frequency phase is obtained by substituting the stationary phase point η_0 into the whole phase defined in (9). Note that the stationary phase point is a function of the range frequency and Doppler frequency. To enhance clarity, we have omitted residual terms arising from the POSP assumption, as they are deemed to be of negligible significance [26].

E. Stationary Phase Point

To obtain a closed-form expression of the 2-D frequency signal (11), we must obtain the derivative of the whole phase [see (9)]

$$(f_c - f_r)\frac{2}{c}\frac{\partial R(\eta)}{\partial\eta} + \frac{1}{\alpha}\frac{\partial f_d(\eta)}{\partial\eta} f_r - f_\eta = 0. \tag{12}$$

As explained in Section II-C, we will use a hyperbolic range equation for $R(\eta)$. Moreover, the Doppler frequency shift $f_d(\eta)$ will be represented as a linear function of the slow time $f_d(\eta) = \beta_d \cdot \eta$ as in [26]. By performing the derivative in (12), we can express that

$$(f_c - f_r)\frac{2}{c}\frac{v_{\text{eq}}^2\eta}{\sqrt{R_0^2 + \left(v_{\text{eq}} \cdot \eta\right)^2}} + \frac{\beta_d}{\alpha} f_r - f_\eta = 0. \tag{13}$$

In previous work [26], (13) is presented for the CryoSat-2 case [26, eq. (8)]. However, in the publication, no more details are provided after this point, leaving the equation as an intermediate form without providing a closed-form expression. Instead, they propose a numerical approach to determine the stationary phase point η_0 by calculating the roots directly in (12). This eliminates the need for making various simplifications listed earlier, such as the hyperbolic range. In contrast, the closed-form filter needs fewer computational operations and requires less memory load. It also reduces the complexity of the processor design. Moreover, the closed-form expression enables a broader analysis of the 2-D frequency waveforms. It is important to remark that these assumptions can lead to a slight degradation in the accuracy of the focused point target response (PTR), as evidenced in the Results section. Building upon their findings, we present a comprehensive analysis that resolves (13) into a concise closed-form expression for the case of Sentinel-6, thereby providing a more complete understanding of its mathematical properties. Thus, after doing some algebra and isolating η from (13), we can express the stationary phase point η_0 in function of the Doppler frequency f_η and the range frequency f_r as

$$\eta_0\left(f_\eta, f_r\right) = \frac{cR_0\left(f_\eta - \beta_d/\alpha \cdot f_r\right)}{2v_{\text{eq}}^2(f_c - f_r)} \frac{1}{D\left(f_\eta, f_r\right)} \tag{14}$$

where $D(f_\eta, f_r)$ is defined as

$$D\left(f_\eta, f_r\right) = \sqrt{1 - \frac{c^2\left(f_\eta - \beta_d/\alpha \cdot f_r\right)^2}{4v_{\text{eq}}^2(f_c - f_r)^2}}. \tag{15}$$

Now, we can use the stationary phase point η_0 to determine the 2-D frequency signal.

F. 2-D Frequency Signal for an Ideal Point Target

After substituting the stationary phase point (14) into (9), the phase of the 2-D frequency signal becomes

$$\theta(\eta_0) = -\frac{2}{c}\left(R_0(f_c - f_r) \cdot D\left(f_\eta, f_r\right) + R_{\text{trk}} \cdot f_r\right). \tag{16}$$

Regarding the along-track frequency envelope $w_\eta(\eta_0)$, the antenna pattern of the radar altimeter follows a Gaussian

model [36]; consequently, the illumination time is understood as the time that a target stays at 3 dB of the antenna footprint

$$T_{\text{ill}} = 0.886\frac{cR_0}{f_c L_a v_g} \tag{17}$$

where L_a stands by the length of the antenna in the azimuth direction. We can compensate for the received energy for the antenna pattern to have a 2-D signal sequence of uniform energy. Thus, for an ideal point target, the 2-D frequency envelope can be defined as

$$W_\eta(f_\eta, f_r) \cdot W_r(f_r) \approx \Pi\left(\frac{f_\eta}{B_D}\right) \cdot \Pi\left(\frac{f_r}{B}\right) \tag{18}$$

where B_D is the Doppler bandwidth of the point target, defined as

$$B_D = \frac{2v_{\text{eq}}^2 f_c T_{\text{ill}}}{cR_0} = 0.886\frac{2v_s}{L_a}. \tag{19}$$

Now, we can combine (16) and (18) to build a closed form of the 2-D frequency signal as defined in (11)

$$S(f_\eta, f_r) = \Pi\left(\frac{f_\eta}{B_D}\right) \cdot \Pi\left(\frac{f_r}{B}\right) \cdot \exp\left[-j\frac{4\pi}{c}\left(R_0 \cdot (f_c - f_r) \cdot D(f_\eta, f_r) + R_{\text{trk}} \cdot f_r\right)\right]. \tag{20}$$

This signal represents one target located at a range R_0 within the illumination time. The omega-K approach aims to apply a single filter to the 2-D frequency waveforms defined in the last equation. The objective is to simultaneously focus on all spatial points within a designated across-track range window and all the observed surfaces during a specific time period. To achieve this, a filter is constructed using a reference range R_{ref}, typically positioned at the center of the designated range window. However, it is crucial to note that residual phase contributions from spatial points around the across-track reference range could lead to defocusing. To address this concern, additional techniques such as the Stolt interpolation method mentioned in [30] could be employed. Section II-H provides an explanation for the minimal impact on defocusing surfaces whose across-track distances deviate from the reference range in altimeter systems, such as Sentinel-6. Within the context of the FF-BP, the impact of applying a phase correction using one unique range for an entire range window has been already studied for the case of CryoSat-2 in [17] and [18].

G. Reference Function Multiply

Once we have a closed-form expression for the 2-D frequency signal, our objective is to correct the phase of the signal, so that when we come back to the 2-D time domain, we obtain the focused signal. To do so, we have to construct a reference function multiply (RFM), proportional to the phase of the input signal

$$\Phi_{\text{RFM}} = \frac{2}{c}\left(R_{\text{ref}} \cdot (f_c - f_r) \cdot D(f_\eta, f_r) + R_{\text{trk}} \cdot f_r\right) \tag{21}$$

where R_{ref} is the aforementioned reference range. Equation (21) is valid within the sampled Doppler interval $|f_\eta| \leq PRF/2$ for the along-track frequency and the chirp bandwidth for the range frequency $|f_r| \leq B/2$. The RFM is then multiplied by the 2-D frequency signal defined in (20)

$$S_{\text{RFM}} = S(f_\eta, f_r) \cdot \exp(j2\pi \cdot \Phi_{\text{RFM}}). \tag{22}$$

H. 2-D PTR

The 2-D frequency signal after filtering can be expressed as

$$S_{\text{RFM}}(f_\eta, f_r, R_{\text{ref}}) = \Pi\left(\frac{f_\eta}{B_D}\right) \cdot \Pi\left(\frac{f_r}{B}\right) \cdot \exp\left[j\frac{4\pi}{c}(R_{\text{ref}} - R_0) \cdot (f_c - f_r) \cdot D(f_\eta, f_r)\right]. \tag{23}$$

When $R_{\text{ref}} = R_0$, the phase is zero and only the envelope of the signal is left. The last step is to perform an IFFT in the along-track dimension and an FFT in the across-track dimension in order to obtain the final focused waveforms in the temporal domain. As expected, the 2-D response over an ideal point target is, therefore, a product of sinc functions

$$s_{\text{PT}}(\eta, t) = \text{sinc}[\eta B_D] \cdot \text{sinc}[tB]. \tag{24}$$

This expression is equivalent to the signal obtained with the backprojection algorithm in [17] and the signal obtained with the FF-WK numerical algorithm in [26]. Therefore, under ideal conditions, the FF-WK closed-form algorithm is equivalent to the backprojection and the FF-WK numerical algorithms. In practice, the approximations that are employed may introduce residual errors that can impact the performance in real scenarios. The Validation section demonstrates that these errors are minor, leading to nearly identical focusing results.

When the reference range R_{ref} is not equal to the range of minimum approach R_0, the phase is not zero, and miss-focusing can occur. If this phase was linear with f_r and f_η, the signal would be focused with a delay shift in range proportional to the linear phase according to the well-known Fourier shift theorem. However, in conventional SAR systems, the term $D(f_\eta, f_r)$ is quadratic. In order to correct this, an extra correction called Stolt interpolation is applied [30]. In an altimetry system, the carrier frequency and pulse bandwidth are typically higher than in SAR satellites. Also, the range window in altimetry is small compared to the sensor to target distance (∼93 m for Sentinel-6 in raw SAR mode, half of it in RMC mode, for an altitude of 1336 km [34]). When comparing the term $D(f_\eta, f_r)$ for typical SAR and altimetry systems, it is found that, in SAR, this term has a significant impact, whereas, in altimetry, it does not. In the context of Sentinel-6, we are examining the phase in (23) when there is a correction error of $R_{\text{ref}} - R_0 = 47$ m, representing the worst case scenario within the range window. This analysis is conducted with respect to the along-track frequency while keeping the range frequency fixed. Our observations reveal that the variation in the linear term is approximately 1 mrad. This small change is consistent enough to be treated as constant. Furthermore, when considering quadratic and higher order terms, their variations are below 0.1 radians. This level of

variation is sufficiently low to consider it negligible. Consequently, in Sentinel-6 radar altimetry, it is unnecessary to implement Stolt interpolation to focus on the remaining across-track positions. In Section IV, a PTR function comparison with and without Stolt interpolation is presented using simulated data over a point target, processed with the WK algorithm, to validate this assumption. Consequently, the range shift of the processed data projected to the focused image is proportional to the difference between the reference range and the actual point target range. We can, therefore, express the 2-D PTR as a function of the difference between the reference range and the range of minimum approach to the target as

$$s_{SL}(\eta, t) = \text{sinc}[\eta B_D] \cdot \text{sinc}[(t-\tau)B] \tag{25}$$

$$\tau = \frac{2 \cdot (R_0 - R_{\text{ref}})}{c} \tag{26}$$

where constant phase terms have been omitted for the sake of simplicity.

I. Range and Azimuth Resolution

The resolution for a sinc-shaped signal is typically defined as the width of the main lobe of the sinc at half of its maximum power [30]. Therefore, the across-track resolution is defined as

$$\delta R_\tau = 0.886 \frac{c}{2B}. \tag{27}$$

For the case of Sentinel-6, the across-track resolution is 0.415 m.

Regarding the along-track direction, the azimuth resolution in distance units is defined as

$$\delta R_{\text{az}} = 0.886 \frac{v_g}{B_D} \gamma_w = \frac{L_a}{2} \frac{v_g}{v_s} \gamma_w \tag{28}$$

where γ_w represents a broadening factor resulting from a frequency processing window. Typically, the term $\gamma_w v_g / v_s$ is approximated to 1, which leads to the recognized definition of azimuth resolution $\delta R_{\text{az}} \approx L_a/2$.

J. Doppler Bandwidth Aliasing Mitigation

In the case of Sentinel-6, the Doppler bandwidth is approximately 10.6 kHz, while the PRF is 9.23 kHz. Consequently, the PRF does not meet the Nyquist theorem. The received energy from Doppler frequencies that are higher than the PRF becomes folded within the limits of the sampled spectrum, introducing aliasing. Fig. 3 showcases the range/azimuth radargram [see Fig. 3(a)] and the corresponding range/Doppler radargram [see Fig. 3(b)] for a simulated point target. We can appreciate how the Doppler spectrum exhibits aliasing due to the low PRF in comparison to the Doppler bandwidth of the point target.

Over scenarios where the flat surface assumption is applicable, such as point targets, open ocean, or sea ice, a straightforward method to mitigate aliasing involves reducing the range window in order to erase aliased ranges (e.g., from 256 to 128 range samples in Fig. 3). This adjustment also helps to reduce the data rate of the satellite [37]. The primary tradeoff with this approach is the loss of information for half

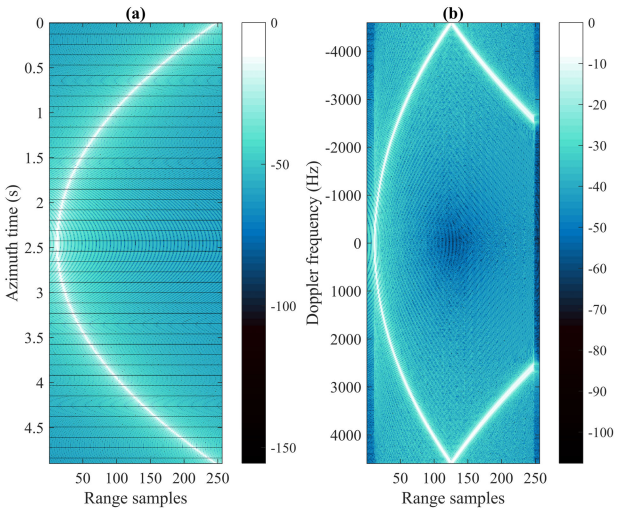

Fig. 3. 2-D power radargram (dB) of a simulated point target for 4.9 s in (a) range/azimuth domain and (b) range/Doppler domain. Due to the limited PRF, we only can process frequencies below PRF/2 = 4.65 kHz. Frequencies higher than half of the PRF become folded within the limits of the sampled spectrum, appearing as interference in higher ranges.

of the range window, which can be acceptable in open ocean and sea ice scenarios, since the most relevant information is before the range cutoff for most applications and is carefully preserved [38], [39]. In addition, there is a loss of along-track resolution since the entire Doppler bandwidth is no longer processed. As the effective range window is reduced, the surface's range migration is constrained, consequently so as to keep the Doppler spectrum below the PRF, free of aliasing. In this case, the broadening factor is $\gamma_w = B_D/\text{PRF} = 1.148$, which means a loss of 14.8% in the along-track resolution with respect to the theoretical maximum. Nevertheless, as the range migration is reduced, the geometric assumptions align more closely with real data, resulting in less degradation of the PTR.

Over other kinds of scenarios where the entire range window is required, such as land-ice or inland scenarios, avoiding aliased ranges through this method becomes unfeasible. In such cases, a more restrictive method involves applying a low-pass filter to the Doppler spectrum to eliminate aliased frequencies. This method, though, comes with the drawback of further reducing along-track resolution. The bandwidth of the low-pass filter is defined as

$$B_{\text{LP}} = 2\text{PRF} - B_D. \tag{29}$$

For Sentinel-6 nominal parameters, the bandwidth of the low-pass filter B_{LP} is approximately 7.75 kHz, which is equivalent to a broadening factor of $\gamma_w = B_D/B_{\text{LP}} = 1.37$, reducing the along-track resolution by a 37% with respect to the theoretical maximum. This is valid assuming the alignment of the antenna beam's center with the point of closest approach to the target, following the orbital simplifications explained in this article. Otherwise, Doppler centroid correction techniques may be applied [30].

III. Algorithm Implementation

In this section, we present a brief explanation of the most important points for the code implementation of the

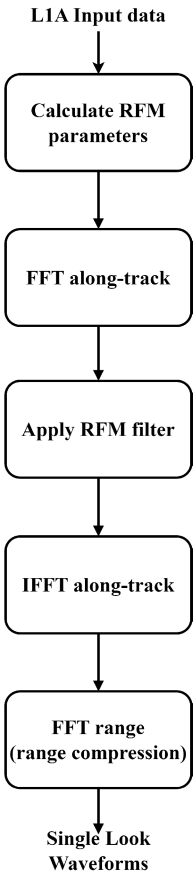

Fig. 4. Omega-K algorithm scheme. The input data pertains to the Sentinel-6 mission Copernicus operational L1A product.

omega-K algorithm. Fig. 4 provides an illustrative depiction of the overall scheme. The input data used for the omega-K processor are obtained from the Sentinel-6 Mission Copernicus Operational L1A product, formatted in NetCDF4. The received echoes in the L1A file are provided in IQ samples, organized in a 3-D structure, specifically in terms of bursts and samples. Each burst corresponds to 64 Ku-band echoes, followed by 1 calibration echo (CAL) and 1 C-band echo. As these CAL and C pulses serve just for calibration purposes, they need to be omitted. In practice, a gap is, therefore, induced every 64 science pulses. The impact on performance and potential solutions to this issue has already been described in [16] and is not assessed in this article.

Each echo contains 256 samples where the range dimension is in the frequency domain; thus, only an FFT in the azimuth direction should be applied to obtain the 2-D frequency-domain signal. Since Sentinel-6 works in interleaved mode, the PRI between bursts is usually coherent; therefore, the burst repetition interval (BRI) is proportional to the PRI. The telemetry data rate is given in terms of burst intervals, so all the waveforms encapsulated in a single burst share the same satellite coordinates and time in the L1A file. The omega-K algorithm is applied to an entire block of echoes. The length of the block can be selected by the user. The construction of the RFM filter, which will be applied to the raw data, entails the calculation of the following parameters.

1) Determine the reference range R_{ref}. Typically, the middle of the window range is selected.
2) Normally, satellites exhibit a linear altitude change, introducing an additional phase term in the 2-D frequency signal because the closest point is not at the nadir anymore. This induces a shift along the satellite direction in the projected data that can be corrected by adding a phase shift term proportional to the altitude rate.
3) Calculate the Doppler rate β_D. To do so, we compute the evolution of the Doppler frequency shift of the surface during all the processed time and then calculate the slope of the resulting function.
4) The effective velocity is computed by calculating the norm of the velocity vector components that are included in the L1A product. It is important to compensate the norm of the velocity by the orbital factor α_E.
5) The range frequency f_r is generated by creating a vector of equally spaced samples. The sampling time is available in the L1A product.
6) Similarly, the along-track frequency f_η is generated by constructing a vector of equally spaced samples. The space between frequencies depends on the PRF, also obtainable from the L1A product.

Once these parameters are determined, the construction of the RFM filter (21) becomes possible. The RFM filter is represented as a matrix, where each column corresponds to a range frequency and each row corresponds to an along-track frequency. Subsequently, an FFT is applied to the input waveforms in the along-track direction to obtain the 2-D frequency signal. Then, the RFM matrix is applied directly to the waveforms as in (22). After that, an IFFT is performed in the along-track frequency domain, followed by an FFT in the range frequency domain (also known as range compression). The output of the processor is a 2-D matrix of the focused surface with respect to the range. Notably, the final range window is linked to the reference range set in the RFM filter. Careful consideration of this range window is crucial to ensure accurate and meaningful results.

Another important aspect when applying an FFT in along-track is the need to have waveforms and pulses equispaced in time. For closed-burst systems such as CryoSat-2 or Sentinel-3, if the BRI is not proportional to the PRI, an interpolation of the data is required to achieve equispaced waveforms among different bursts. In contrast, satellites such as Sentinel-6 operate in interleaved mode and are likely to have equispaced data during the entire processed time. Still, the PRF of such interleaved systems is dynamic as it needs to adjust to the variable satellite altitude, leading to variations in the periodicity of pulse reception throughout the illumination time. Different strategies may be employed to address such changes, such as interpolating the data to maintain a constant PRI. Moreover, it is important to know that the ignored CAL pulses induce replicas in the azimuth projection [16].

Finally, despite our emphasis on capturing all the surfaces visible to the satellite throughout the processed period, it is important to note the presence of transient zones at the margin of a block of echoes. These transient zones arise from the finite

TABLE I
SENTINEL-6 POSEIDON-4 ALTIMETER INSTRUMENT PARAMETERS

Sentinel-6 Parameters	
Carrier Frequency	13.575 GHz
Pulse bandwidth	320 MHz
PRF (nominal)	9.23 kHz
Sampling Frequency (nominal)	395 MHz
Pulse duration	32 μs
Range Samples	256
Mean Altitude	1336 km
Orbital velocity (nominal)	7.2 km/s

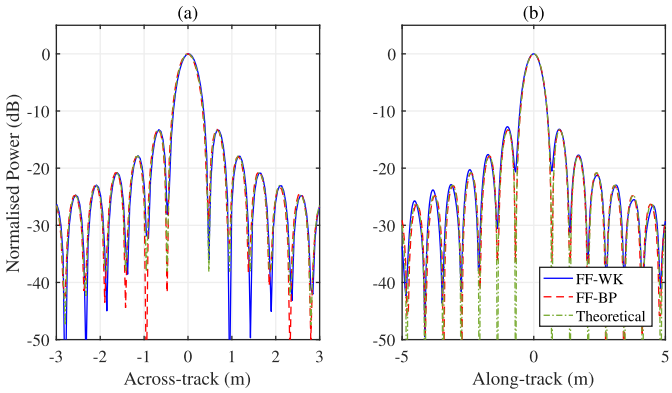

Fig. 5. Simulated PTR at the point of maximum power. FF-WK, FF-BP, and theoretical models are shown. (a) Across-track cut. (b) Along-track cut.

length of the data. Specifically, the surface at the beginning and end of the observation period does not experience full illumination. Indeed, if we consider the multiplication in the frequency domain (RFM filter) as equivalent to a convolution in time, it is clear that the output of the filter at the initial and concluding pulses is not complete, inducing edge effects. As a result, it is necessary to exclude these incompletely illuminated regions from the dataset of the radar image being focused upon.

IV. VALIDATION

Four different validation exercises have been considered in order to evaluate the performance of the omega-K algorithm. First, a simulator has been developed to validate the PTR of the processor against simulated data and to verify the unnecessity of the Stolt interpolation for the case of Sentinel-6. Second, real data from Sentinel-6 passes over a transponder and a corner reflector have been used to evaluate the real PTR and the long-term stability of the processor over point targets. Finally, an open ocean scenario is used to evaluate the performance of the processors over distributed targets. The omega-K processor used to derive all the results was developed following the steps outlined in Section III.

A. Response Over Simulated Point Target

To validate the theoretical model and assess the performance of the algorithm, a simulated scenario has been created and analyzed. These simulated data accurately replicate all stages of the Sentinel-6 receiver system, including the expected orbit and all the parameters within the Poseidon-4 altimeter instrument [10]. These parameters are outlined in Table I.

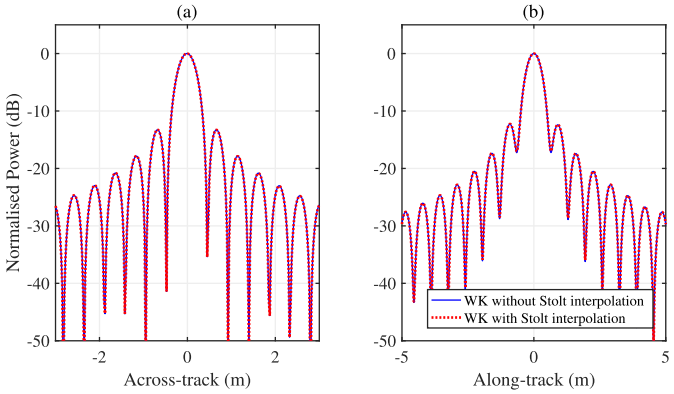

Fig. 6. Stolt interpolation comparison: PTR at the point of maximum power. The PTR is assessed for cases when interpolation is applied and when it is not. The worst case scenario has been evaluated, applying a reference range 47 m away from the range of the point target. Both responses show good agreement. (a) Across-track cut. (b) Along-track cut.

Consequently, the radar geometry closely resembles an actual Sentinel-6 product. The primary advantage of employing this simulation is that the input signal for the omega-K processor can be precisely modeled according to (3). Therefore, any potential noise or interference that typically occurs in real-world scenarios does not affect the performance of the algorithm. The simulated data have been processed over 3.4 s, which is almost the maximum that we can set to apply the omega-K filter. Moreover, a zero-padding factor of 8 has been applied to the range dimension to improve visualization. The along- and across-track cuts for the FF-WK closed-form, FF-BP, and the theoretical model are depicted in Fig. 5. It can be seen that all the signals are consistent with both FF-WK and FF-BP matching the expected theoretical model. The along-track resolution for the FF-WK closed-form method is 0.577 m, whereas, for the FF-BP, it is 0.565 m. The expected theoretical resolution is 0.56 m; therefore, the FF-WK closed-form algorithm presents an error of 2%, and the FF-BP algorithm presents an error of 1% with respect to the theoretical value.

In addition, we utilized simulated data to assess the impact of Stolt interpolation on the omega-K algorithm. For this analysis, we processed the data applying the Stolt interpolation, as described in [30], and also performed the analysis without applying Stolt interpolation. Fig. 6 presents a comparison of both PTR. In this case, there is a difference of 47 m from the reference range to the real target range. This value corresponds to the maximum difference found in the Sentinel-6 range window between the center and the edges when operating in raw SAR mode, being half of it when operating in the RMC mode. Notably, there is an imperceptible difference between the two cuts. Still, we have found that applying the Stolt interpolation improves the along-track resolution from 0.577 to 0.572 m, a relative improvement of 0.87%, which we consider of negligible significance. Regarding the peak-to-sidelobe ratio (PSLR), differences are less than 0.1 dB.

B. Response Over Real Point Targets

Transponders and corner reflectors are key elements for radar altimetry external calibration [23], [40]. On the one

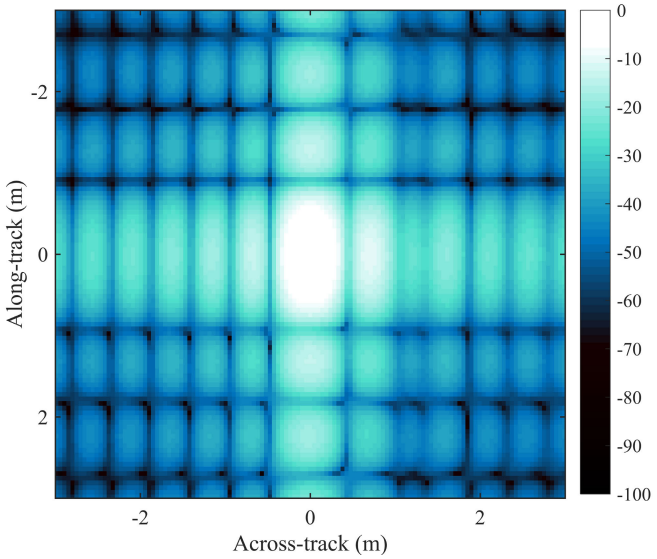

Fig. 7. FF-WK 2-D PTR image corresponding to a Sentinel-6 pass on January 6, 2021, over the Crete transponder [40]. The x-axis represents the range with respect to the point target. The y-axis represents the point distance with respect to the point target. Normalized power in decibels.

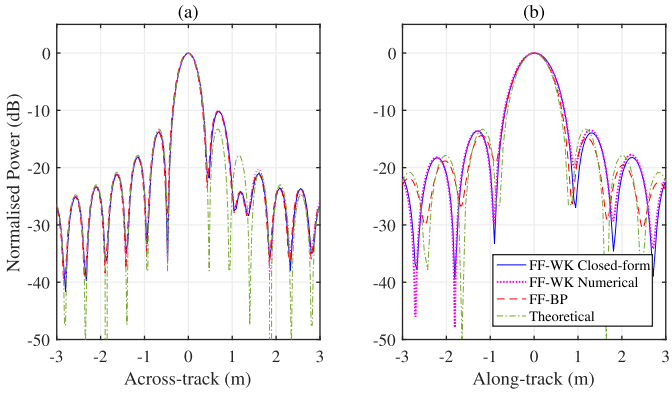

Fig. 8. PTR functions over the transponder in Crete corresponding to the Sentinel-6 pass on January 6, 2021. The responses obtained by the FF-WK and FF-BP processors have been centered at the point of maximum power. (a) Across-track PTR. (b) Along-track PTR.

TABLE II

TRANSPONDER PTR VALUES ARE PRESENTED FOR THREE PROCESSORS: FF-WK CLOSED-FORM, FF-WK NUMERICAL, AND FF-BP. THE PROCESSED TIME FOR ALL ALGORITHMS IS 2.4 s

Transponder	FF-WK CF	FF-WK NM	FF-BP
PSLR Left Across (dB)	13.56	13.56	13.56
PSLR Right Across (dB)	10.00	10.00	10.00
PSLR Left Along (dB)	13.59	13.59	14.39
PSLR Right Along (dB)	13.95	13.40	14.78
Across-track Resolution (m)	0.42	0.42	0.42
Along-track Resolution (m)	0.79	0.79	0.76

hand, transponders, as active elements, offer a high signal-to-noise ratio (SNR) and signal-to-clutter ratio (SCR) compared to passive corner reflectors despite their complexity. On the other hand, passive elements such as corner reflectors are noisier but can provide very precise measurements due to their intrinsic simplicity and long-term stability. In this section, results from a single Sentinel-6 pass over a transponder are used to compare the omega-K PTR response over a point target against a backprojection algorithm and the omega-K numerical approach in [26] adapted to Sentinel-6. Moreover, results of a series of Sentinel-6 flights over a corner reflector are analyzed to evaluate the long-term performance of the processor.

1) PTR Over a Transponder: Fig. 7 shows the 2-D PTR image from a Sentinel-6 pass on January 6, 2021, over the transponder of Crete [40], processed within 2.6 s. This duration represents the maximum observable time limited by the received power from the transponder in this pass. Fig. 8 provides visualizations of the across- and along-track sections relative to the point of maximum energy for the three processors, where the PTR response obtained by an FF-SAR backprojection processor and an FF-WK numerical processor are also plotted for comparison confirming the good agreement, especially in the range case. In power terms, the PSLR for the across-track response measures 13.56 and 10 dB for the left and right lobes, respectively. Such an asymmetry, also captured by the other processors, is a well-known feature of this transponder [41]. The width of the primary lobe at -3 dB is 0.42 m, coinciding with the theoretical range resolution. The PSLR of the along-track evolution for the omega-K closed-form algorithm is 13.59 dB for the left secondary lobe and 13.95 dB for the right secondary lobe. The omega-K numerical processor presents a PSLR of 13.59 dB for the left secondary lobe and 13.4 dB for the right secondary lobe. The backprojection algorithm presents a PSLR of 14.39 dB for the left secondary lobe and 14.78 dB for the right secondary lobe. In terms of along-track resolution, the width of the main lobe is marginally broader in both omega-K processors, as the main lobe at -3 dB for the omega-K algorithm is 0.79 m, slightly wider than the theoretical resolution, which is 0.72 m for 2.6 s of the processed time. Thus, the omega-K processor has a loss in the along-track resolution of 9.7% with respect to the theoretical value. In this case, the backprojection algorithm gets closer to the theoretical value, 0.76 m with a loss of 5.6%. Refer to Table II for a comprehensive overview of all the obtained outcomes presented in this section. This table presents a summary of the results derived from the transponder outcomes using the three processors. The parameters considered in this table include across-track resolution, along-track resolution, and PSLR.

2) Range Measurement Stability: The long-term behavior of the omega-K processor is assessed by evaluating its stability in terms of range measurements on a sequence of passes over the isardSAT's corner reflector located in Montsec (Catalonia) [23]. In this case, we have considered a processing time of 3.3 s in order to avoid aliasing in the Doppler frequencies. Fig. 9 depicts the across- and along-track cuts for a pass over the corner reflector on October 25, 2021. To better visualize the across-track evolution, an oversampling factor of 8 has been applied. We can see that the shape of the sinc in the along-track dimension for the omega-K case is not as perfect as in the transponder case. As the corner reflector SCR is low compared to the transponder, the received energy for the point target is lower, making the phase of the received signal more noisy and making it more difficult for the omega-K algorithm to obtain the expected sinc shape as predicted by the theory due to the approximations made for the algorithm,

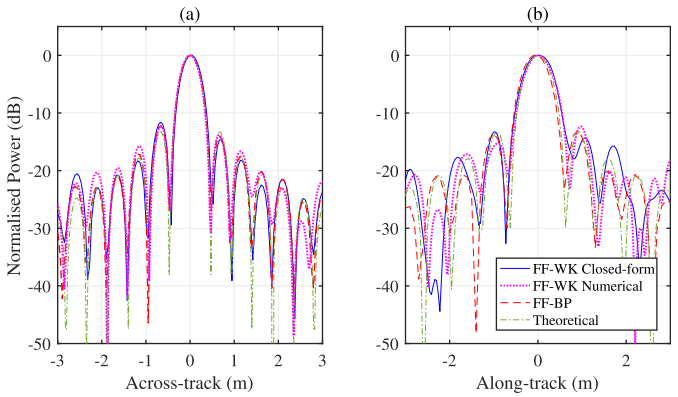

Fig. 9. PTR functions over the Corner reflector in Montsec corresponding to the Sentinel-6 pass on October 25, 2021. The responses obtained by the FF-WK and FF-BP processors have been centered at the point of maximum power. (a) Across-track PTR. (b) Along-track PTR.

as the real point target signal differs from the theoretical model. However, the response of the point target is still clearly visible. Quantitatively, the PSLR for the across-track cut is measured at 11.5 and 14.8 dB, for the left and right lobes, respectively. The width of the main lobe at −3 dB is 0.42 m. On the other hand, the left secondary lobe in the along-track cut reaches 13.2 dB, and the right secondary lobe reaches 14.31 dB. The width of the main lobe at −3 dB is 0.65 m, which represents a loss of 14% in the along-track theoretical resolution (0.57 m). In this case, the FF-WK numerical approach improves the performance of the closed-form algorithm, getting an along-track resolution of 0.63 m, which means a loss of 10.5% with respect to the theoretical. The backprojection algorithm gets closer to the theoretical value, 0.6 m, representing a loss of only 5.3%. In contrast with the transponder case, the long-term behavior is observed in Fig. 10, which depicts the evolution of the range bias between September 2021 and July 2022. In total, 28 passes have been processed. All of them were computed with the omega-K and the backprojection algorithms. For this study, the range samples have been oversampled by a factor of 128, which means that every sample is spaced 2.96 mm. The average range bias for the omega-K closed-form case is 2.99 cm, and the standard deviation is 1.23 cm, while, for the omega-K numerical processor, the average range bias is 3.10 cm, and the standard deviation is 1.22 cm. The average range bias for the backprojection case is 3.20 cm, and the standard deviation is 0.93 cm, showing full consistency between methods and comparable precision. The approximately 3-cm range bias can be attributed to the residual uncertainty in the reflector vertex determination, as detailed in [23]. Refer to Table III for a comprehensive overview of all the obtained outcomes presented in this section. This table presents a summary of the results derived from the corner-reflector measurement campaign for both processors, encompassing both theoretical and empirical outputs. The parameters considered in this table include across- and along-track resolutions, PSLR, and range measurement stability.

C. Distributed Target: Open Ocean

We have conducted an analysis of the performance of the FF-WK over open ocean focusing on two well-known

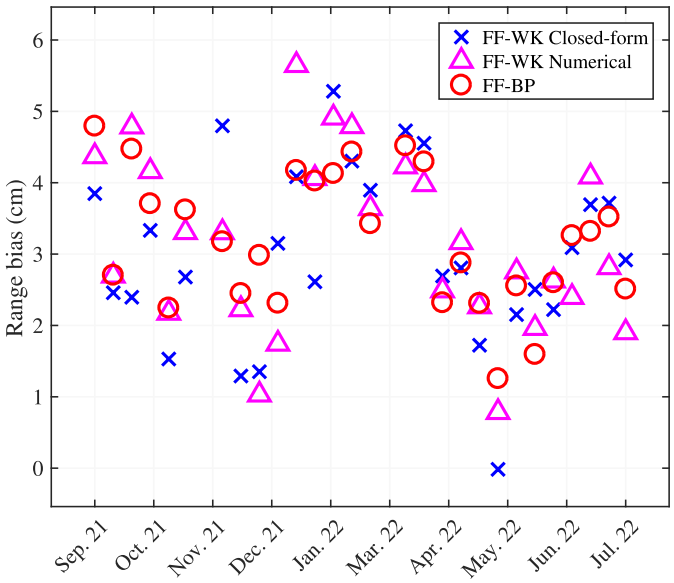

Fig. 10. Measured range bias with Sentinel-6 over the Montsec corner reflector computed with FF-WK closed-form, FF-WK numerical, and FF-BP processors during one year of measurements.

TABLE III

CORNER REFLECTOR RANGE MEASUREMENT STABILITY VALUES ARE PRESENTED FOR THREE PROCESSORS: FF-WK CLOSED-FORM, FF-WK NUMERICAL, AND FF-BP. RANGE BIAS MEASUREMENTS WERE CONDUCTED FOR 28 PASSES BETWEEN SEPTEMBER 2021 AND JULY 2022. THE PERFORMANCE OF PSLR AND RESOLUTION HAS BEEN DONE FOR A SINGLE PASS THAT OCCURRED ON OCTOBER 25, 2021

Corner Reflector	FF-WK CF	FF-WK NM	FF-BP
Range Bias STD (cm)	1.23	1.22	0.93
Range Bias Average (cm)	3.00	3.10	3.20
PSLR Left Across (dB)	11.5	11.90	11.90
PSLR Right Across (dB)	14.8	13.75	13.75
PSLR Left Along (dB)	13.20	15.20	13.75
PSLR Right Along (dB)	14.31	11.10	13.20
Across-track Resolution (m)	0.42	0.42	0.42
Along-track Resolution (m)	0.65	0.63	0.60

geophysical parameters: the sea surface height (SSH) and the significant wave height (SWH). The objective of this validation is to compare the results of FF-SAR algorithms (omega-K and backprojection) with the Sentinel-6 Mission Copernicus Operational L2 Product (delay/Doppler). Approximately 12 km of Sentinel-6 data were processed: three passes from November 15, 2021, February 22, 2022, and January 14, 2022, were selected in order to include a representative set of different SWHs from 2.6 to 4.1 m. The latitudes covered by these passes range between 25.0° and 28.6°.

The processing integration time was set to 2 s. The FF-SAR SL waveforms were multilooked in order to achieve a final spacing of 306 m in along-track, making these waveforms comparable to the DDP product. Finally, the range samples were oversampled by a factor of 2. The retracking stage was applied by adapting the delay/Doppler analytical retracker defined in [38] to operate with FF-SAR waveforms, as done in [42]. This process was employed to derive the SSH and SWH for each spatial point.

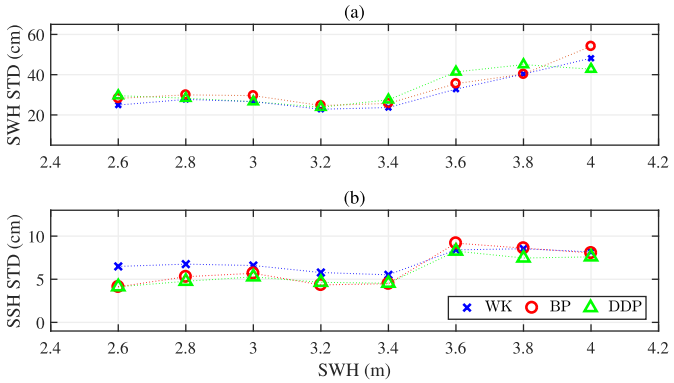

Fig. 11. Analysis of Sentinel-6 over an open ocean scenario: (a) standard deviation of SWH and (b) standard deviation of SSH as functions of SWH using FF-WK, FF-BP, and delay/Doppler methods. The standard deviation of SSH and SWH is consistent across all three approaches.

After that, we proceeded to compute the standard deviation of SSH and SWH parameters as functions of the SWH. To achieve this, we calculate the standard deviations by averaging the variances of the obtained parameters from 20 consecutive power waveforms, known as the 20-Hz standard deviations. This calculation is performed after removing any trends and outliers present. Likewise, we determine the averages of the derived SWH, followed by sorting and grouping them into bins of 0.2 m each. Fig. 11 showcases the standard deviation for both parameters in function of the SWH bins, showing consistent behavior among all the processors.

V. Applications

The reduced execution time of FF-WK in comparison to time-based backprojection processors, coupled with its enhanced along-track resolution compared to unfocused techniques, such as DDP, may be of interest for applications where vast extensions of data must be processed while maintaining high along-track resolution. In this section, we identify two specific applications: swell retrieval and sea ice monitoring.

A. Swell Retrieval

One of the primary goals of the Sentinel-6 mission is to monitor the evolution of the ocean over time, where radar altimetry is used to gather crucial geophysical parameters, such as sea level and wind speed, among others. However, the vast size of the ocean poses a major challenge when processing large amounts of data. Within this domain, one notable use is the monitoring of swell [43]. While swell retrieval using SAR techniques has been conducted for numerous years utilizing satellites such as Sentinel-1 [44], observing swells through radar altimetry has been a pending research primarily due to the unique nadir-pointing geometry characteristic of radar altimeters, along with the restricted spatial resolution that existed prior to the development of FF-SAR algorithms. The utilization of fully focused algorithms now permits the examination of swell waves through the analysis of intensity modulations in the waveform tail. Given that the geometry of radar altimetry diverges from that of other remote sensing systems such as conventional SAR, the interpretations and limitations associated with swell retrieval also differ significantly, ushering in new perspectives. Swell observations derived from altimetry hold significance as they enhance the spatial–temporal sampling of oceanic swell systems. In addition, their monitoring aids in the cross-calibration of swell observations originating from various platforms [45]. In the context of radar altimetry, the monitoring of swells assumes a critical role in discerning the influence of wind waves and swell within the sea-state bias [46]. Moreover, the process of swell flagging plays a vital role in identifying potential biases present in retrackers [47]. Recent work [28] has demonstrated the FF-SAR capabilities to map these spectra catching swell signals down to the meter scale. In addition, ongoing projects such as SARWAVE by the European Space Agency (ESA) [48] are currently involved in research efforts to provide a more detailed understanding of changes in swell intensity. This includes the incorporation of sublooking and its associated cross-spectra analysis, aimed at elevating the accuracy of retrieving swell-wave parameters.

In order to show the performance of the omega-K, an L1A Sentinel-6 product from May 25, 2022, has been analyzed. In this case, 2 s of the processed time was utilized. Following the SL processing, along-track focused points were multilooked at 30 m. Furthermore, range samples have been oversampled by a factor of 2. Fig. 12 illustrates the 2-D response of an open ocean track with FF-WK. The ripples observed in along-track at the tails of the ocean waveforms are indicative of potential swell in the image. Without delving excessively into intricate details, Fig. 13 illustrates the 2-D omega-K cross-spectra derived from the data shown in Fig. 12, following the methodology outlined in [28]. Preferably, we would like to have a single bright point indicating the direction of the swell. Instead, the 2-D cross-spectra exhibit ambiguities in both directions, originated from the inherent characteristics of nadir-pointing antennas employed in altimeter systems. This design necessitates the altimeter to observe both sides of the ground track [28]. As an introduction to one of the potential applications of the omega-K processor, its capability to process open ocean scenarios with swell is presented while acknowledging that further research is required to fully explore its capabilities in this area for the potential achievements of omega-K in swell retrieval applications.

B. Sea Ice Applications

Another application that involves the processing of large volumes of data and will benefit from a highly efficient FF-SAR algorithm is sea ice monitoring. Sea ice applications, such as lead or iceberg detection, heavily rely on the utilization of high-resolution algorithms and computationally efficient processors to achieve optimal results. Although Sentinel-6 is not specifically designed to study ice scenarios in polar regions, an upcoming satellite mission, CRISTAL, will continue the primary objective of the CryoSat-2 mission and take advantage of an open burst scheme to produce high-resolution results [49].

For this analysis, a Sentinel-6 L1A product from September 5, 2021, has been selected. The pass crosses latitudes between $-65.05°$ and $-65.01°$, near the Antarctic Peninsula. The data have been processed with the FF-WK, using 2 s of the processed time. After processing, the surface

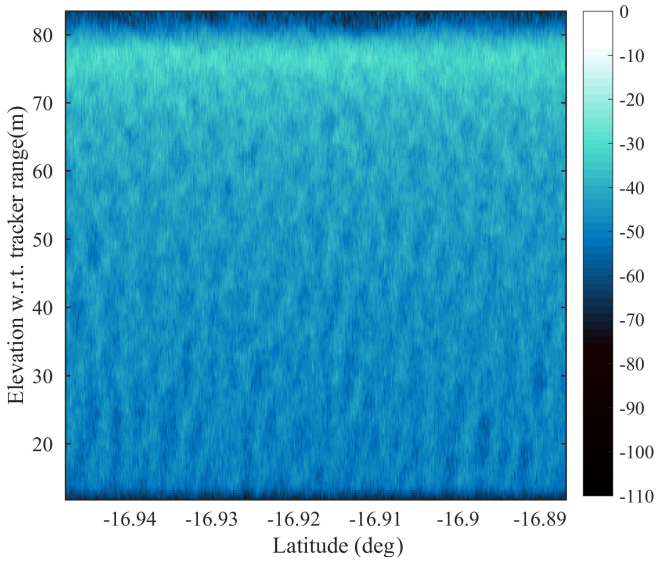

Fig. 12. FF-WK 2-D image from an open ocean Sentinel-6 track. Swell-induced intensity modulations can be appreciated. Normalized power in decibels.

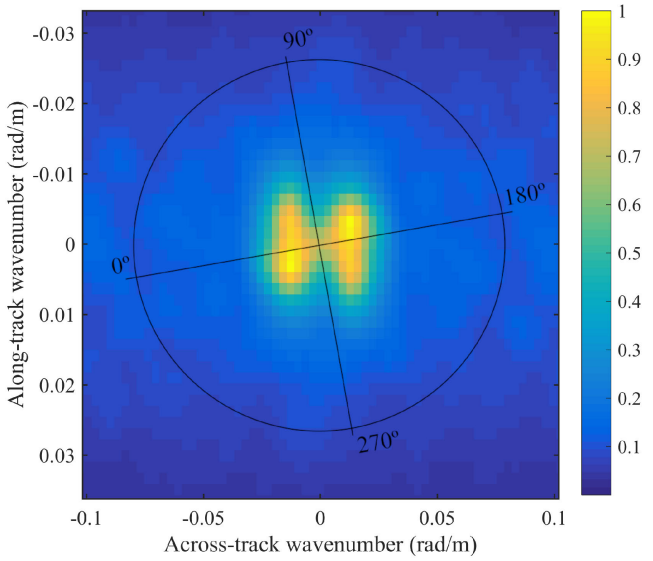

Fig. 13. FF-WK 2-D cross-spectra. The ambiguities that appear in the image are due to the nature of the nadir-pointing antenna from the altimeter.

points have been averaged in order to obtain a multilooked surface of 30 m. Furthermore, range samples have been oversampled by a factor of 2. Fig. 14 depicts a 2-D image processed with FF-WK for a sea ice scenario. As observed, leads can be easily distinguished from the ice zones due to the different backscatter energy of water compared to the energy reflected by ice. Leads can have dimensions in the order of a few meters, thus making high-resolution algorithms such as backprojection and omega-K crucial for such applications. Fig. 15 presents a comparison between the optical image and the FF-WK 2-D radargram. The nadir-pointing orientation of the antenna introduces across-track ambiguities in the FF-WK 2-D response, making it challenging to precisely geolocate leads within the same across-track range. However, prominent leads are clearly visible, and a correlation can still be established between the optical image and the leads detected in the altimeter radargram. The impact of the nadir-pointing

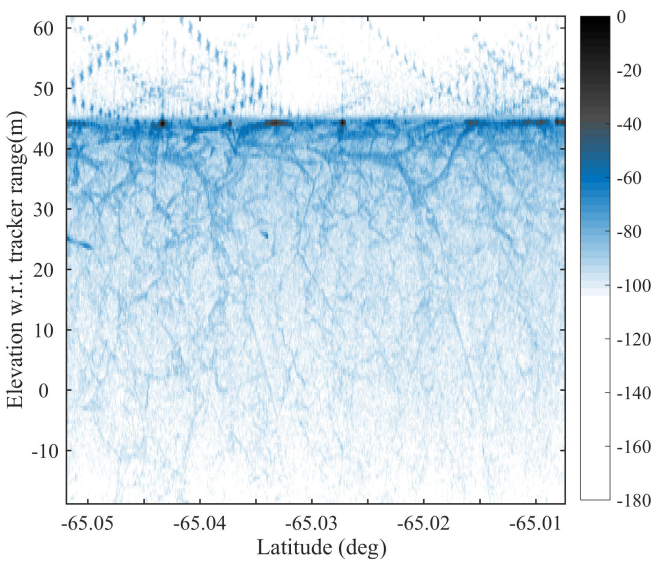

Fig. 14. FF-WK 2-D image from a sea ice Sentinel-6 track, where the distribution of off-nadir leads is clearly recognized. Normalized power in decibels. The parabolic features observed above the leading edge are caused by along-track replicas induced by periodic discontinuities in the pulse transmission chain for calibration purposes [16].

antenna is evident in lead #1, as depicted in Fig. 15. The radargram illustrates an image of the latitude (x-axis) and range (y-axis), causing leads that intersect the track, such as lead #1 mentioned earlier, to appear "folded" in the 2-D altimeter radargram. It is essential to note that this limitation does not render certain applications impossible, and using image processing techniques should allow for high-resolution classification. For instance, water extent estimation from leads remains feasible [39]. Thanks to that, we can quantify the total amount of water surface and get better probability density functions of narrow leads, which is crucial to calibrate sea-ice models [50], [51], [52]. In addition, successful lead detection and iceberg detection can still be achieved [29], [53]. Despite the challenges posed by across-track ambiguities, the data obtained from the FF-WK 2-D radargram remain valuable for various analyses and studies related to sea ice monitoring and characterization.

VI. Computational Efficiency

The main feature of the omega-K processor over the backprojection algorithm is the reduction in the number of operations required to obtain an SL waveform. In the case of backprojection, the process involves compensating the phase of each received pulse and integrating them all in order to obtain an SL waveform. In contrast, the omega-K processor necessitates the application of an FFT in the along-track direction and the use of a 2-D frequency filter to focus all the SL waveforms covered during the processed time at once. This fundamental distinction yields a significant enhancement in computational efficiency. The number of operations that FF-BP requires to correct the phase of the 2-D waveforms and focus the data can be expressed in terms of the number of along-track points N_{ill} and the number of samples N_r [26], as shown in the following:

$$N_{\text{BP}} = N_{\text{ill}} \cdot \left(4 + \log_2 N_r\right). \tag{30}$$

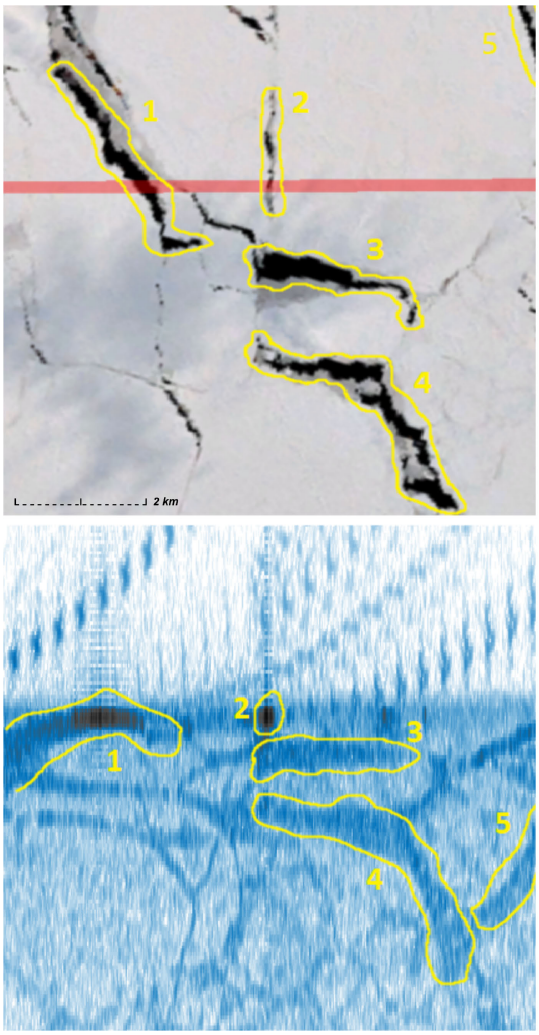

Fig. 15. (Top) Sentinel-2 image and (bottom) Sentinel-6 FF-WK 2-D image corresponding to a zoomed-in area of Fig. 14. Many of the leads in the optical image can be recognized in the altimeter radargram.

For the omega-K processor, we have a data block containing N_{ill} echoes that are processed at once. Therefore, the number of operations required per sample and data block can be expressed as follows:

$$N_{\text{WK}} = 2 \cdot \left(\frac{N_p}{N_{\text{ill}}} + 1 + 2 \cdot \log_2 N_{\text{ill}} + \log_2 N_r \right). \tag{31}$$

In this context, N_p represents the number of operations required to compute essential input parameters such as equivalent velocity or Doppler rate. The computation of the equivalent velocity is straightforward and only needs two to three arithmetic operations for each data block. On the other hand, determining the Doppler rate requires about N_{ill} operations for each data block. Furthermore, the constant term of 1 accounts for the multiplication of the RFM filter with the 2-D frequency data. The second term corresponds to the FFT and IFFT operations applied to the along-track dimension. Finally, the last term is for the range compression process at the end of the focus. The multiplication factor of 2 applied to all operations originates from the presence of transient zones at the start and end of the data. These initial and final segments contain data points that cannot be entirely utilized for analysis, as the satellite's field of view does not encompass the complete observational dataset for those specific points. In this case, the FF-SAR omega-K processor has been designed in such a way that half of the observed surface is erased in the end.

Just to provide an overview of the data scale that we are handling, let us consider the case of Sentinel-6. During the processed time of 2 s, we have around 18 000 echoes of 256 range samples to process. In order to focus all the received pulses, approximately 216 000 operations are required for the FF-SAR backprojection processor, whereas, for the omega-K closed-form algorithm, only 74 operations are needed. For the case of the omega-K numerical approach, using [26, eq. (16)] with Sentinel-6 parameters, 922 operations are needed. This indicates that the FF-WK closed-form method requires around 3000× less operations than the FF-BP processor and around 13× less operations than the FF-WK numerical algorithm. It is important to note that the three algorithms could be optimized, for example, using parallel computing, which means that the number of operations could be reduced. Even with that, the enhancement in the execution time of the omega-K method is quite significant. It is essential to note that, in the backprojection algorithm, the number of operations increases linearly with the number of along-track pulses, whereas, in the omega-K algorithm, the number of operations increases on a logarithmic scale. This implies that the omega-K algorithm becomes more efficient as we compute more surface, which is intuitive since the main objective of the FF-WK is to reduce the number of operations required to focus one data block of echoes simultaneously.

In order to compare the computational efficiency of both FF processors, a series of tests using a Sentinel-6 product pass over the corner reflector with different configuration parameters has been done. The execution times for FF-WK and FF-BP with varying configurations are presented in Table IV. The tests have been done with an Intel[1] Core[2] i7-4600M 2.90-GHz single-core CPU with 16 GB of RAM. This experiment is presented to provide a general idea of the computational efficiency of both algorithms, as the results may vary depending on the code development, optimization techniques applied, and the parallelization strategy if any. The strong difference in terms of execution time is observed in all the tests, where the FF-WK is faster at least with a factor close to 2000 in the worst case. As we can observe in the second and third columns, reducing the along-track step size offers significant advantages to backprojection. By doing so, we effectively decrease the number of received pulses being processed. As mentioned earlier, the number of processed pulses directly impacts the number of operations required for backprojection, leading to a linear increase. Conversely, in the omega-K algorithm, this effect is logarithmic, resulting in a more gradual growth in processing operations with respect to the number of processed pulses. It is important to recall that these numbers may not align precisely with theoretical expectations due to various execution implications, including differences in code implementation for each processor.

[1]Registered trademark.
[2]Trademarked.

TABLE IV
EXECUTION TIME OF BOTH FF PROCESSORS FOR DIFFERENT TESTING PARAMETERS AIMED AT COMPARING THE EFFICIENCY OF THE OMEGA-K ALGORITHM VERSUS THE CLASSIC BACKPROJECTION ALTERNATIVE

Parameters				
Range zero-padding	1	1	1	2
Along-track step (m)	0.68	0.68	1.37	0.68
Observation Time (s)	1	2	2	2
Ground track length (km)	6	12	12	12
Results				
FF-WK execution time (s)	1.54	2.9	2.68	3
FF-BP execution time (s)	5520	10870	5515	11957

VII. DISCUSSION

The FF-WK presented in this article, validated with a long series of point target measurements, shows the viability of this kind of algorithm for future radar altimeter missions and the fast data reprocessing of current ones.

Assessing the results of range measurements using a corner reflector, combined with observations taken from dispersed targets such as the open ocean, provides important insights into the accuracy and precision capabilities of the omega-K system. As shown, the omega-K algorithm closely reproduces the results of the backprojection technique, showing slightly lower performance, while still being a good option for remote sensing purposes. The omega-K algorithm holds potential for a wide array of applications that were once limited by the slow computational performance of existing algorithms such as the backprojection. The reduction in execution time achieved by our algorithm unlocks opportunities for new applications. Specifically, this improved computational efficiency opens the door for the generation of global products in areas such as swell retrieval and sea ice, where time and precise data analysis are of importance. Also, other applications, such as global-scale in-land water processing, may benefit from fast algorithms [1], [18]. Finally, the almost real-time processing capability shown in Section VI with just a single CPU core opens the path for future in-flight real-time processing of radar altimetry data, which holds interest for many of the applications introduced.

VIII. CONCLUSION

The FF-WK presented in this article offers an alternative to current high-resolution radar altimetry algorithms, such as the FF-SAR backprojection [17] and the 2-D frequency domain [26].

The algorithm proposed has undergone a full validation process. The validation results over point targets, including simulated data and real data from transponders and a corner reflector, demonstrate precision and accuracy comparable to its equivalent time-domain alternative. Moreover, the results show the algorithm's versatility in various environments (open ocean and sea ice) and its potential applications, including a better estimation of swell, as well as lead and iceberg detection. Furthermore, it has been demonstrated that a 2-D frequency-based omega-K algorithm decreases substantially the execution time with respect to time-based processors, such as the backprojection algorithm.

Finally, there are still potential areas for improvement and further investigation. Identifying limitations is crucial for improving the algorithm's performance and broadening its abilities. It is important to study how orbit assumptions affect the accuracy and precision of the algorithm. In addition, we should conduct an analysis of how to optimize algorithm parameters, such as the along-track windowing and the mitigation of replicas, taking into account the specific application and any limitations inherent to the algorithm. Moreover, we need to explore strategies for addressing issues such as the synchronization of the PRF changes to have equispaced data in each block of echoes that will be processed for the WK algorithm. In terms of applications, exploring specific application requirements is essential for enhancing the algorithm. Also, future research efforts should also concentrate on refining the implementation and optimization of the processor, as operational applications where global products are crucial pose a significant challenge in the future.

ACKNOWLEDGMENT

The authors thank Ester Vendrell (isardSAT, S.L.) for her advice during the writing phase of this document. Sergi Hernández-Burgos would like to express his gratitude to the Delft University of Technology (TU Delft) for hosting him for three months as part of his Ph.D. degree.

REFERENCES

[1] S. Vignudelli, A. Scozzari, R. Abileah, J. Gómez-Enri, J. Benveniste, and P. Cipollini, "Chapter Four—Water surface elevation in coastal and inland waters using satellite radar altimetry," in *Extreme Hydroclimatic Events and Multivariate Hazards in a Changing Environment*, V. Maggioni and C. Massari, Eds. Amsterdam, The Netherlands: Elsevier, 2019, pp. 87–127.

[2] A. Tarpanelli and J. Benveniste, "Chapter Eleven—On the potential of altimetry and optical sensors for monitoring and forecasting river discharge and extreme flood events," in *Extreme Hydroclimatic Events and Multivariate Hazards in a Changing Environment*, V. Maggioni and C. Massari, Eds. Amsterdam, The Netherlands: Elsevier, 2019, pp. 267–287.

[3] K. A. Giles, S. W. Laxon, and A. P. Worby, "Antarctic sea ice elevation from satellite radar altimetry," *Geophys. Res. Lett.*, vol. 35, no. 3, pp. 1–5, Feb. 2008, doi: 10.1029/2007gl031572.

[4] A. Mémin, T. Flament, F. Rémy, and M. Llubes, "Snow- and ice-height change in Antarctica from satellite gravimetry and altimetry data," *Earth Planet. Sci. Lett.*, vol. 404, pp. 344–353, Oct. 2014.

[5] A. Cazenave, H. Palanisamy, and M. Ablain, "Contemporary sea level changes from satellite altimetry: What have we learned? What are the new challenges?" *Adv. Space Res.*, vol. 62, no. 7, pp. 1639–1653, Oct. 2018.

[6] L. Gray, D. Burgess, L. Copland, T. Dunse, K. Langley, and G. Moholdt, "A revised calibration of the interferometric mode of the CryoSat-2 radar altimeter improves ice height and height change measurements in Western Greenland," *Cryosphere*, vol. 11, no. 3, pp. 1041–1058, May 2017.

[7] M. Grgic and T. Bašić, "Radar satellite altimetry in geodesy—Theory, applications and recent developments," in *Geodetic Sciences—Theory, Applications and Recent Developments*. Zagreb, Croatia: Univ. Zagreb, 2021, ch. 5, pp. 1–18. [Online]. Available: https://www.intechopen.com/books/9870

[8] *CryoSat-2 Mission Summary*. Accessed: Dec. 7, 2023. [Online]. Available: https://www.eoportal.org/satellite-missions/cryosat-2#preparatory-campaigns

[9] *Sentinel-3 Mission Summary*. Accessed: Dec. 7, 2023. [Online]. Available: https://sentinels.copernicus.eu/web/sentinel/missions/sentinel-3/overview/mission-summary

[10] *Sentinel-6 Mission Summary*. Accessed: Dec. 7, 2023. [Online]. Available: https://sentinels.copernicus.eu/web/sentinel/missions/sentinel-6/overview

[11] R. K. Raney, "The delay/Doppler radar altimeter," *IEEE Trans. Geosci. Remote Sens.*, vol. 36, no. 5, pp. 1578–1588, Sep. 1998.

[12] C. Donlon, R. Cullen, L. Giulicchi, M. Fornari, and P. Vuilleumier, "Copernicus Sentinel-6 Michael freilich satellite mission: Overview and preliminary in orbit results," in *Proc. IEEE Int. Geosci. Remote Sens. Symp.* , Jul. 2021, pp. 7732–7735.

[13] K. R. Raney, "CryoSat SAR-mode looks revisited," in *Proc. ESA Living Planet Symp.*, vol. 686, H. Lacoste-Francis, Ed. 2010, p. 216.

[14] R. K. Raney, "Maximizing the intrinsic precision of radar altimetric measurements," *IEEE Geosci. Remote Sens. Lett.*, vol. 10, no. 5, pp. 1171–1174, Sep. 2013.

[15] C. Gommenginger, C. Martin-Puig, A. Laiba, and R. Raney, "Review of state of knowledge for SAR altimetry over ocean. Report of the EUMETSAT JASON-CS SAR mode error budget study," Nat. Oceanogr. Centre, Southampton, U.K., Tech. Rep. 14/749304, 2013.

[16] S. Amraoui et al., "FFSAR replica removal algorithm for closed-burst data," Collecte Localisation Satellites (CLS), Tech. Rep., 2022.

[17] A. Egido and W. H. F. Smith, "Fully focused SAR altimetry: Theory and applications," *IEEE Trans. Geosci. Remote Sens.*, vol. 55, no. 1, pp. 392–406, Jan. 2017.

[18] M. Kleinherenbrink, M. Naeije, C. Slobbe, A. Egido, and W. Smith, "The performance of CryoSat-2 fully-focussed SAR for inland water-level estimation," *Remote Sens. Environ.*, vol. 237, Feb. 2020, Art. no. 111589.

[19] Y. Yuan, "Estimation of river width with fully-focused SAR altimetry data," in *Proc. AGU Fall Meeting Abstr.*, 2019, pp. 1–22.

[20] F. Schlembach et al., "Benefits of fully focused SAR altimetry to coastal wave height estimates: A case study in the North Sea," *Remote Sens. Environ.*, vol. 289, May 2023, Art. no. 113517.

[21] Hydrocoastal Consortium Team (HCA), "HCA impact assessment report," ESA, Europe, Tech. Rep. 3.1, 2023.

[22] A. Egido, D. C. Vandemark, and H. Feng, "An evaluation of fully focused SAR altimetry for coastal applications," in *Proc. AGU Fall Meeting Abstr.*, 2018, pp. 1–4.

[23] F. Gibert et al., "A trihedral corner reflector for radar altimeter calibration," *IEEE Trans. Geosci. Remote Sens.*, vol. 61, pp. 1–8, 2023.

[24] L. M. H. Ulander, H. Hellsten, and G. Stenstrom, "Synthetic-aperture radar processing using fast factorized back-projection," *IEEE Trans. Aerosp. Electron. Syst.*, vol. 39, no. 3, pp. 760–776, Jul. 2003.

[25] A. Fasih and T. Hartley, "GPU-accelerated synthetic aperture radar backprojection in CUDA," in *Proc. IEEE Radar Conf.*, May 2010, pp. 1408–1413.

[26] P. Guccione, M. Scagliola, and D. Giudici, "2D frequency domain fully focused SAR processing for high PRF radar altimeters," *Remote Sens.*, vol. 10, no. 12, p. 1943, Dec. 2018.

[27] M. Scagliola, P. Guccione, and D. Giudici, "Fully focused SAR processing for radar altimeter: A frequency domain approach," in *Proc. IEEE Int. Geosci. Remote Sens. Symp.*, Jul. 2018, pp. 6699–6702.

[28] O. Altiparmaki, M. Kleinherenbrink, M. Naeije, C. Slobbe, and P. Visser, "SAR altimetry data as a new source for swell monitoring," *Geophys. Res. Lett.*, vol. 49, no. 7, Apr. 2022, Art. no. e2021GL096224.

[29] D. Dettmering, A. Wynne, F. Müller, M. Passaro, and F. Seitz, "Lead detection in polar oceans—A comparison of different classification methods for Cryosat-2 SAR data," *Remote Sens.*, vol. 10, no. 8, p. 1190, Jul. 2018.

[30] I. G. Cumming and F. H. Wong, *Digital Processing of Synthetic Aperture Radar Data: Algorithms and Implementation*. Norwood, MA, USA: Artech House, 2005.

[31] J. MacArthur, "Design of the SEASAT-A radar altimeter," in *Proc. OCEANS*, 1976, pp. 222–229.

[32] H. Breit, T. Fritz, U. Balss, M. Lachaise, A. Niedermeier, and M. Vonavka, "TerraSAR-X SAR processing and products," *IEEE Trans. Geosci. Remote Sens.*, vol. 48, no. 2, pp. 727–740, Feb. 2010.

[33] J.-W. Park and J.-S. Won, "An efficient method of Doppler parameter estimation in the time-frequency domain for a moving object from TerraSAR-X data," *IEEE Trans. Geosci. Remote Sens.*, vol. 49, no. 12, pp. 4771–4787, Dec. 2011.

[34] C. J. Donlon et al., "The Copernicus Sentinel-6 mission: Enhanced continuity of satellite sea level measurements from space," *Remote Sens. Environ.*, vol. 258, Jun. 2021, Art. no. 112395.

[35] C. Bender, S. Orszag, and S. Orszag, *Advanced Mathematical Methods for Scientists and Engineers I: Asymptotic Methods and Perturbation Theory* (Advanced Mathematical Methods for Scientists and Engineers). Berlin, Germany: Springer, 1999.

[36] S. Dinardo et al., "Sentinel-6 MF Poseidon-4 radar altimeter in-flight calibration and performances monitoring," *IEEE Trans. Geosci. Remote Sens.*, vol. 60, 2022, Art. no. 5119316.

[37] M. Kuschnerus et al., "Sentinel-6 Poseidon-4 RMC mode processing and expected performance," Delft Univ. Technol., Delft, The Netherlands, Tech. Rep., 2018.

[38] C. Ray et al., "SAR altimeter backscattered waveform model," *IEEE Trans. Geosci. Remote Sens.*, vol. 53, no. 2, pp. 911–919, Feb. 2015.

[39] F. Müller, D. Dettmering, W. Bosch, and F. Seitz, "Monitoring the Arctic seas: How satellite altimetry can be used to detect open water in sea-ice regions," *Remote Sens.*, vol. 9, no. 6, p. 551, Jun. 2017.

[40] S. Mertikas et al., "A permanent infrastructure in Crete for the calibration of Sentinel-3, Cryosat-2 and Jason missions with a transponder," in *Proc. ESA Living Planet Symp.*, 2013, pp. 2–13.

[41] S. Amraoui, S. P. Mertikas, M. Fornari, A. Garcia-Mondeja, M. Scagliola, and F. Boy, "New results of Sentinel-6 transponder working group," in *Proc. 3rd Sentinel-6 Validation Team Meeting*, 2021, pp. 1–18.

[42] F. Gibert et al., "Results of the dragon 4 project on new ocean remote sensing data for operational applications," *Remote Sens.*, vol. 13, no. 14, p. 2847, Jul. 2021.

[43] F. Collard, F. Ardhuin, and B. Chapron, "Monitoring and analysis of ocean swell fields from space: New methods for routine observations," *J. Geophys. Res., Oceans*, vol. 114, no. 7, pp. 1–15, Jul. 2009.

[44] H. Wang, A. Mouche, R. Husson, and B. Chapron, "Dynamic validation of ocean swell derived from Sentinel-1 wave mode against buoys," in *Proc. IEEE Int. Geosci. Remote Sens. Symp.*, Jul. 2018, pp. 3223–3226.

[45] Y. Zhang, Y. Wang, and Q. Xu, "On the nonlinear mapping of an ocean wave spectrum into a new polarimetric SAR image spectrum," *J. Phys. Oceanogr.*, vol. 50, no. 11, pp. 3109–3122, Nov. 2020.

[46] F. Collard, L. Marié, F. Nouguier, M. Kleinherenbrink, F. Ehlers, and F. Ardhuin, "Wind-wave attenuation in Arctic sea ice: A discussion of remote sensing capabilities," *J. Geophys. Res., Oceans*, vol. 127, no. 7, 2022, Art. no. e2022JC018654.

[47] F. Schlembach et al., "Round Robin assessment of radar altimeter low resolution mode and delay-Doppler retracking algorithms for significant wave height," *Remote Sens.*, vol. 12, no. 8, p. 1254, Apr. 2020.

[48] *SARWAVE Project*. Accessed: Dec. 7, 2023. [Online]. Available: https://www.sarwave.org/

[49] M. Kern et al., "The Copernicus polar ice and snow topography altimeter (CRISTAL) high-priority candidate mission," *Cryosphere*, vol. 14, no. 7, pp. 2235–2251, Jul. 2020.

[50] A. Herman, M. Wenta, and S. Cheng, "Sizes and shapes of sea ice floes broken by waves—A case study from the East Antarctic Coast," *Frontiers Earth Sci.*, vol. 9, May 2021, Art. no. 655977.

[51] A. A. Denton and M.-L. Timmermans, "Characterizing the sea-ice floe size distribution in the Canada basin from high-resolution optical satellite imagery," *Cryosphere*, vol. 16, no. 5, pp. 1563–1578, May 2022.

[52] T. W. K. Armitage and R. Kwok, "SWOT and the ice-covered polar oceans: An exploratory analysis," *Adv. Space Res.*, vol. 68, no. 2, pp. 829–842, Jul. 2021.

[53] J. Tournadre, N. Bouhier, F. Boy, and S. Dinardo, "Detection of iceberg using delay Doppler and interferometric Cryosat-2 altimeter data," *Remote Sens. Environ.*, vol. 212, pp. 134–147, Jun. 2018.

Sergi Hernández-Burgos received the M.S. degree in telecommunication engineering from the Universitat Politècnica de Catalunya, Barcelona, Catalonia, in 2020, where he is currently pursuing the Ph.D. degree in signal theory and communications, codirected by isardSAT-Cat, Barcelona.

In 2019, he joined isardSAT, S.L., Barcelona, as a Research and Development Engineer. His main activities are the research, development, and implementation of altimetry data processing algorithms.

Ferran Gibert received the M.S. degree in aerospace engineering and the Ph.D. degree in aerospace science and technology from the Universitat Politècnica de Catalunya, Barcelona, Catalonia, in 2011 and 2016, respectively. His Ph.D. degree was focused on the design of thermal diagnostics experiments for the LISA Pathfinder mission.

From 2016 to 2018, he completed post-doctoral research at the University of Trento, Trento, Italy, from where he supported the LISA Pathfinder operations and data analysis phase. Since June 2018, he has been a Research and Development Engineer with isardSAT, S.L., Barcelona, being currently involved in the development of algorithms for radar altimeter processors.

Antoni Broquetas (Member, IEEE) was born in Barcelona, Catalonia, in 1959. He received the Engineering and Doctor Engineering degrees in telecommunication engineering from the Universitat Politècnica de Catalunya (UPC), Barcelona, in 1985 and 1989, respectively, where his dissertation was on microwave tomography.

In 1986, he was a Research Assistant with Portsmouth Polytechnic, Portsmouth, U.K., where he was involved in propagation studies. In 1987, he joined the Department of Signal Theory and Communications, School of Telecommunication Engineering, UPC. From 1998 to 2002, he was the Subdirector of Research of the Institute of Geomatics, Barcelona. Since 1999, he has been a Full Professor with UPC, where he is involved in research on radar imaging and remote sensing. From 2003 to 2006, he was the Director of the Department of Signal Theory and Communications, UPC. From 2005 to 2009, he proposed and comanaged the Knowledge To Market (K2M) Program at UPC to support university spin-offs. He has published more than 200 papers on microwave tomography, radar, inverse synthetic aperture radar (ISAR), synthetic aperture radar (SAR) systems, SAR processing, and interferometry. His research interests include SAR calibration techniques, ground moving target indication (GMTI) SAR performance analysis, geostationary earth orbit search and rescue (GEOSAR), and mmW ground-based SAR, in support of future SAR missions and radar remote sensing innovation.

Marcel Kleinherenbrink received the master's degree from the Faculty of Aerospace Engineering, Delft University of Technology, Delft, The Netherlands, in 2013, and the Ph.D. degree from the Faculty of Civil Engineering and Geoscience, Delft University of Technology, in 2018, with a focus on the observation of sea-level change and vertical land motion from space.

He specializes in the observation of the ocean surface using active radar instruments. In 2019, he became involved in the Earth Explorer 10 Mission, Harmony, for which he implements forward models, investigates inversion strategies, and provides performance estimates. Since 2018, he has been involved in numerous European Space Agency (ESA) projects related to future missions and novel retrieval algorithms for ocean observations.

Adrián Flores De la Cruz received the M.S. and Ph.D. degrees in telecommunication engineering from the Polytechnic University of Cartagena, Murcia, Catalonia, in 2014 and 2019, respectively.

From 2017 to 2019, he was a Cal/Val Engineer with Hisdesat SA, Madrid, Catalonia, where he worked on the PAZ Mission. Since March 2019, he has been a Research and Development Engineer with isardSAT, S.L., Barcelona, Catalonia, working on the development and implementation of data processing techniques with a special focus on instrumental calibration.

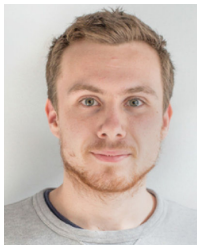

Adrià Gómez-Olivé received the bachelor's degree in telecommunication technologies and service engineering from the Universitat Politècnica de Catalunya, Barcelona, Catalonia, in 2022, where he is currently pursuing the M.S. degree in advanced telecommunication technologies.

He joined isardSAT-Cat, Barcelona, in 2021. His tasks include the implementation and handling of processing techniques of synthetic aperture radar (SAR) altimetry data for calibration and monitoring tools and the analysis of inland water level and extension from altimetry data measurements.

Albert García-Mondéjar received the M.S. degree in telecommunication engineering from the Universitat Politècnica de Catalunya, Barcelona, Catalonia, in 2009.

He joined isardSAT-Cat, Barcelona, in 2011, where he is currently a Senior Altimetry Engineer and the Research and Development Manager. He led isardSAT-UK, Guildford, U.K., from 2014 to 2019. He has wide experience in algorithm development, from L0 to L2, for synthetic aperture radar (SAR) altimetry missions. His fields of expertise include the improvement of L1 algorithms, instrument calibration, science multimission activities, and innovative methods to improve performances over complex scenarios.

Mònica Roca i Aparici received the M.S. degree in electronics and telecommunication engineering from the Universitat Politècnica de Catalunya, Barcelona, Catalonia, in 1995.

She has been the Founder and the Director of isardSAT Group, Barcelona, since its foundation in 2006. She has been actively involved in the design and development of onboard and on-ground processing algorithms (including instrument calibration, Level 1 processing, and up to Level 2 retracking algorithms) mainly from radar altimetry instruments onboard European Space Agency (ESA) satellites and in all satellite mission phases and for all ESA Earth Observation missions that embark a radar altimeter for more than 25 years. She also worked at ESA/European Space Research and Technology Centre (ESTEC), Noordwijk, The Netherlands, from 1994 to 2003, as a Radar Performance Engineer of ENVISAT RA-2.